Received: 4 March 2025 | Revised: 14 August 2025 | Accepted: 22 October 2025

DOI: 10.1002/aic.70133

AIChE JOURNAL

RESEARCH ARTICLE

Thermodynamics and Molecular-Scale Phenomena

Low Parsons–Zobel slope of metal–solution interfaces: A theoretical comparison of three causes

Weiqiang Tang[1,2] | **Shuangliang Zhao**[3] | **Michael Eikerling**[2,4] | **Jun Huang**[2,4]

[1]Interdisciplinary Research Center for Sustainable Energy Science and Engineering (IRC4SE2), School of Chemical Engineering, Zhengzhou University, Zhengzhou, China

[2]Institute of Energy Technologies, IET-3: Theory and Computation of Energy Materials, Forschungszentrum Jülich GmbH, Jülich, Germany

[3]Guangxi Key Laboratory of Petrochemical Resource Processing and Process Intensification Technology and School of Chemistry and Chemical Engineering, Guangxi University, Nanning, China

[4]Theory of Electrocatalytic Interfaces, Faculty of Georesources and Materials Engineering, RWTH Aachen University, Aachen, Germany

Correspondence
Weiqiang Tang, Interdisciplinary Research Center for Sustainable Energy Science and Engineering (IRC4SE2), School of Chemical Engineering, Zhengzhou University, 450001 Zhengzhou, China.
Email: wqtang@zzu.edu.cn
Jun Huang, Institute of Energy Technologies, IET-3: Theory and Computation of Energy Materials, Forschungszentrum Jülich GmbH, 52425 Jüich, Germany.
Email: ju.huang@fz-juelich.de

Funding information
Initiative and Networking Fund of the Helmholtz Association, Grant/Award Number: VH-NG-1709; European Research Council Starting Grant, Grant/Award Number: 101163405; National Natural Science Foundation of China, Grant/Award Number: 22108070; Young Elite Scientists Sponsorship Program by CAST, Grant/Award Number: 2022QNRC001

Abstract

Rational design of electrochemical energy conversion and storage devices hinges on a fundamental understanding of the electrical double layer (EDL) at the electrode–electrolyte interface. The classical Gouy–Chapman–Stern model of EDL predicts a unity Parsons–Zobel (PZ) slope, which is derived from the relation between inverse measured capacitance and inverse Gouy–Chapman capacitance. However, recent experiments on metals such as Au and Pt have revealed ultrahigh capacitances and ultralow PZ slopes, markedly deviating from the classical model. In this study, we employ density-potential functional theoretic models to systematically compare three mechanisms: surface roughness, nonspecific ion attraction, and ion chemisorption with partial charge transfer. Our analysis reveals that only ion chemisorption fully accounts for the ultrahigh double layer capacitance and ultralow PZ slopes. The gleaned insights into the EDL on transition metals are informative for understanding local reaction environment in electrochemical energy conversion and storage devices.

KEYWORDS
double layer capacitance, ion chemisorption, nonspecific ion adsorption, Parsons–Zobel slope, surface roughness

1 | INTRODUCTION

Metal–solution interfaces are fundamental to many chemical engineering processes, from electrocatalysis to energy conversion and storage.[1–3] When an electrolyte solution encounters a charged metal surface, a nanoscale region termed electrical double layer (EDL) is formed. The properties of EDL are very different from those of the bulk metal and bulk electrolyte solution, exhibiting characteristic spatiotemporal fluctuations in the concentration of ions, solvent molecules, and electric potential. Under equilibrium, the differential double layer capacitance C_{dl} is widely used as a lumped parameter, embodying information about the EDL structure.[1,4–6]

For an ideally planar EDL without charge transfer reactions or chemisorption, the Gouy–Chapman–Stern (GCS) model provides an effective description of the inhomogeneous distributions of ion

density and electric potential within the EDL.[7–9] In the GCS model, the C_{dl} is obtained from two capacitors connected in series:

$$\frac{1}{C_{dl}}=\frac{1}{C_{GC}}+\frac{1}{C_H}, \quad (1)$$

where C_{GC} and C_H are the Gouy–Chapman and Helmholtz capacitance, respectively. C_H is considered to be independent of ionic concentrations but could exhibit a dependence on electrode potential.[10] The validity of the classical GCS model is often evaluated using the Parsons–Zobel (PZ) analysis, which plots $1/C_{dl}$ vs. $1/C_{GC}$ at various electrolyte concentrations.[11] A straight line with a unit slope verifies the GCS model, and the corresponding intercept corresponds to $1/C_H$. The classical GCS model is well-established for mercury electrodes, as shown in Figure 1A, because the mercury surface is atomically smooth and ideally polarizable in a wide potential range.[11] Kornyshev, Sphor, and Vorotyntsev presented an in-depth PZ analysis of the mercury EDLs not only at the potential of zero charge (PZC), as usually presented, but also at a series of surface charge densities.[20]

However, the GCS model falls short for the EDLs at electrocatalytic metals such as Ag, Au, Pt. In 1989, Valette[13] measured C_{dl} curves of Ag(111) in three aqueous electrolytes: KPF_6, NaF, and $NaClO_4$. At the PZC, the PZ slopes are 0.877, 0.676, and 0.649 for Ag(111)-KPF_6, Ag(111)-NaF, and Ag(111)-$NaClO_4$ aqueous solution interfaces, respectively, see the data reproduced in Figure S1. Valette attributed

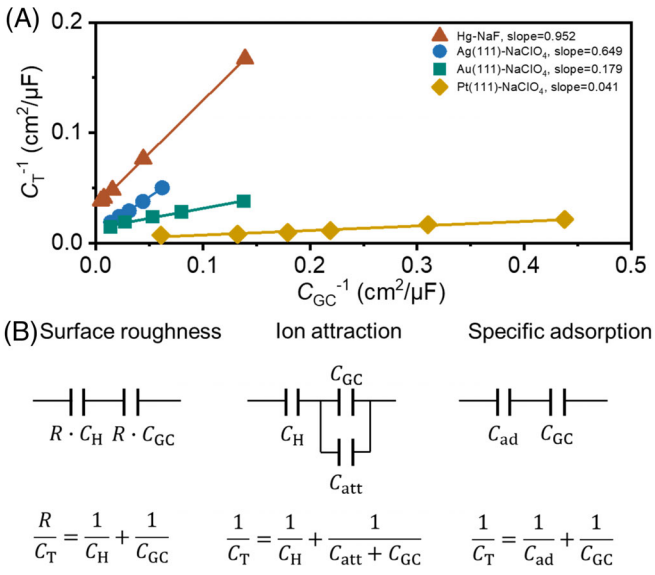

FIGURE 1 Ultralow Parsons–Zobel (PZ) slopes observed in experiments and existing interpretations. (A) Experimental PZ plots of Hg,[12] Ag(111),[13] Au(111),[14] and Pt(111)[14] at the potential of zero charge. (B) Equivalent circuits and the corresponding expressions for the total capacitance C_T which is used uniformly for all examined cases considering surface roughness,[15,16] ion attraction at the metal–solution interfaces,[17] and specific adsorption.[18,19] It is understood that $C_T = C_{dl}$ in absence of chemisorption. R is the roughness factor. C_H, C_{GC}, C_{ad} and C_{att} are the Helmholtz capacitance, Gouy–Chapman capacitance, specific adsorption capacitance, and "ion–surface attraction capacitance," respectively.

this deviation to specific anion adsorption with a sequence of $ClO_4^- > F^- > PF_6^-$ in strength.[13] In 1993, Hamelin et al.[15] also measured C_{dl} curves at an Ag(111)-NaF aqueous solution interface and reported a PZ slope of 0.65 at the PZC. They attributed the smaller PZ slope to surface roughness of the solid electrode. Subsequently, they proposed a method to correct the roughness effects on the PZ slope, as depicted in Figure 1B. In this model, the apparent Debye length is inversely proportional to the roughness factor, resulting in a positive correlation between C_{GC} and roughness factor. Consequently, a low surface roughness factor of 1.05 leads to a PZ slope as low as 0.6.[16]

Recently, Ojha et al.[14] measured the C_{dl} curves at Au(111) and Pt(111) in aqueous solutions and found ultralow PZ slopes of 0.179 and 0.041 for Au(111)-$NaClO_4$ and Pt(111)-$NaClO_4$ interfaces, as shown in Figure 1A. Moreover, the PZ slopes of Pt(111) in contact with $NaClO_4$, $LiClO_4$, $CsClO_4$, $NaCH_3SO_3$, and LiF electrolytes were found to be nearly identical, suggesting that the PZ slopes for Pt(111) are largely insensitive to the nature of the electrolyte.[21] These ultralow PZ slopes cannot be explained by surface roughness or specific adsorption of electrolyte ions. To explain this behavior, the authors modified the GCS model by introducing weak, nonspecific, attractive forces between the electrolyte ions and the metal surface.[17] Figure 1B shows their equivalent circuits and the corresponding expression for the total capacitance C_T in the presence of ion attraction at the metal–solution interfaces. It is noted that C_T is used uniformly for all examined cases throughout the paper and it is understood that $C_T = C_{dl}$ in absence of chemisorption. The "ion attraction capacitance" due to short-range attractive ion–surface interactions is in parallel with C_{GC}, which effectively increases C_T and decreases the PZ slope.[17,21] Schmickler[18,19] proposed an alternative theory invoking an ion-specific adsorption capacitance, C_{ad}, in series with C_{GC}, as shown in Figure 1B. The ion chemisorption is described using Langmuir adsorption isotherms, correlating the electric potential at the adsorption site, ϕ_{ad}, with the charge density on the metal surface via the Frumkin corrections. As the adsorbates are charged, the potential drop between the metal surface and the adsorbate layer, $\phi_M - \phi_{ad}$, is proportional to the magnitude of the charge carried on the adsorbates, $|q_{ad}|$. A self-consistent solution results in adsorption capacitance C_{ad} and Gouy–Chapman capacitance C_{GC}. The addition of C_{ad} to C_T significantly decreases the PZ slope. The Schmickler theory is, however, at odds with the ion-nonspecific nature of PZ slopes.

Currently, there is no consensus on which origin, that is, surface roughness, ion attraction, or specific adsorption, is the main cause of the small PZ slopes. Important insights could be provided by a theoretical model of the EDL that describes metal electronic effects, surface roughness, ion attraction, specific chemisorption of ions in a unified and computationally efficient way. In the past years, we have been developing a density-potential functional theory (DPFT) of EDLs, integrating an orbital-free quantum mechanical description of delocalized electrons in the metal, a classical statistical field description of the electrolyte solution, and empirical potential functions of the short-range metal–electrolyte interactions.[22–25] The aptness of DPFT for describing planar metal–solution interfaces without specific adsorption has been verified in previous work. In Reference

25, the C_{dl} curves of Ag(111)-KPF_6 aqueous solution interface have been analyzed using a DPFT model. The model has been employed to decipher the origin of the solvent effect on the PZC of Au(111)-nonaqueous solution interfaces, highlighting the crucial role of interfacial permittivity distribution on the electron spillover and thus the PZC.[26] Very recently, DPFT was extended to treat ion chemisorption using the Anderson–Newns Hamiltonian,[27] implicitly describing the hybridization of ion orbitals and metal electronic structure. In this study, specific ion adsorption does not involve partial charge transfer, while chemisorption does and leads to partially charged adsorbates.

Recent theoretical work by Hedley et al.[28] found that interfacial water structuring can cause deviations from ideal PZ slopes via accumulation of ions in the inner layer of the EDL. Incorporating the insight of Hedley et al.,[28] the DPFT framework provides a unified description of metal electronic effects, chemisorption, and short-range metal–ion interactions. This unified approach allows for a more detailed decomposition of the individual contributions to PZ slope and double layer capacitance. Building on its capability in treating metal electronic effects, chemisorption, and short-range metal–ion interactions, we employ the DPFT model to understand the origins of the ultralow PZ slopes and ultrahigh capacitance. In the next section, the computational models and methods are introduced, followed by verifying the DPFT model using PZ plots measured at planar Ag(111)-KPF_6 aqueous interfaces. The DPFT model is then employed to examine the impact of surface roughness, ion attraction, and ion chemisorption on PZ slopes and capacitance, respectively. The article concludes with a discussion of the most likely origin of the ultralow PZ slopes at Ag, Au and Pt electrodes.

2 | COMPUTATIONAL MODELS AND METHODS

2.1 | DPFT framework

Within the DPFT framework,[22–25] the grand potential Ω of the metal–solution interface is given by:

$$\Omega = F_{qm} + F_c + F_{int} - \int \left(\sum_i n_i \tilde{u}_i \right), \; i = e, a, c, s, \tag{2}$$

where F_{qm} includes the kinetic, and exchange-correlation energy of a quantum mechanical electron liquid. According to the Kohn–Sham scheme,[29] F_{qm} is to be divided as follows,

$$F_{qm} = T_{ni}[n_e, \nabla n_e, \ldots] + U_{XC}[n_e, \nabla n_e, \ldots], \tag{3}$$

where $T_{ni}[n_e, \nabla n_e, \ldots]$ is the kinetic energy of non-interacting (besides classical electrostatic interactions) electrons, which can be described by the Thomas–Fermi–von Weizsäcker theory.[30–32] $U_{XC}[n_e, \nabla n_e, \ldots]$ is the exchange-correlation energy. In this work, the Perdew–Burke–Ernzerhof (PBE) functional is employed.[30,33]

F_c is the Helmholtz free energy of an inhomogeneous fluid composed of charged particles and solvent molecules that interact via long-range Coulombic force and short-range forces. In a previous work[24] following the original work of Lue et al.,[34] the complexity of treating short-range forces is addressed by introducing a reference system that accounts for all forces except the Coulombic force, whose properties are assumed to be known *a priori*. This treatment leads to,

$$F_c = \int d^3 r f_c, \tag{4}$$

where f_c is the volumetric Helmholtz free energy,

$$f_c = -\frac{1}{2}\epsilon_{hf}(\nabla\phi)^2 + \sum_{l=1}^{N_C} n_l \left(\delta(l \in M) q_l \phi - \delta(l \in S) \beta^{-1} \ln \frac{\sinh(\beta p_l |\nabla\phi|)}{\beta p_l |\nabla\phi|} \right) + \sum_{l=1}^{N_C} \beta^{-1} n_l \left(\ln(n_l \Lambda_l^3) - 1 \right) + \Phi_{ex}(\{n_l\}) + (n_{cc} - n_e) e_0 \phi. \tag{5}$$

Here, the first term on the right-hand side represents the self-energy of the electric field, which is derived from the Hubbard–Stratonovich transformation of particle–particle interactions.[35–38] ϵ_{hf} and ϕ are the permittivity and the electric potential, respectively. Notice that ϵ_{hf} is known to vary spatially as the electrode and the electrolyte possess different permittivities, denoted by $\epsilon_{hf,M}$ and $\epsilon_{op,S}$, respectively. In practical simulations, ϵ_{hf} is interpolated as

$$\epsilon_{hf}(x) = \epsilon_{hf,M} + \frac{\epsilon_{op,S} - \epsilon_{hf,M}}{2}(1 - \mathrm{erf}(-2(x - x_M))), \tag{6}$$

here, x_M denote the metal boundary. In the metal phase, the account for all electrons within the theory renders $\epsilon_{hf,M}$ equivalent to the vacuum permittivity. Given that the orientational polarization of the solvent has been considered, $\epsilon_{op,S}$ primarily accounts for the electronic polarization of ions and solvent molecules. The second term represents the potential energies of charged particles in solution, arising from particle–particle Coulombic interactions.[39] $\beta = (k_B T)^{-1}$ with k_B the Boltzmann constant, T the temperature. p_l is the dipole moment. The symbol $\delta(l \in M)$ is equal to one for monopolar (M) charged particles, for example, cations and anions, and zero otherwise, while $\delta(l \in S)$ is equal to one for dipolar solvent molecules (S) and zero otherwise. The third term represents the Gibbs free energy of an ideal-gas reference system, where Λ_l is the thermal wavelength of particle l. The fourth term, $\Phi_{ex}(\{n_l\})$, signifies the excess Gibbs free energy when the reference system deviates from an ideal gas system.[34,40] Within this theoretical framework, the steric effect of particles is encompassed by this term, with its description facilitated by Bikerman theory.[41–44] A more advanced description is provided by the modified fundamental measure theory (MFMT),[45–47] the exploration of which will be undertaken in the future work. The fifth term represents the Hartree energy of electrons and cationic cores of the electrode, where n_{cc} is the charge density of metal cationic cores.

The short-range interactions F_{int} between the metal surface and ions and solvent molecules in the electrolyte solution are described using the Morse potential.[48]

$$w_l = D_l\left\{\exp\left[-2\beta_l\left(d\left(\vec{r}\right)-d_{0,l}\right)\right]-2\exp\left[-\beta_l\left(d\left(\vec{r}\right)-d_{0,l}\right)\right]\right\}, \quad (7)$$

with D_l being the well depth, β_l a coefficient controlling the well width, $d\left(\vec{r}\right)$ the distance from $\vec{r}$ to the metal surface, $d_{0,l}$ the equilibrium distance between the molecule and the metal surface.

The last term $\int\left(\sum_i n_i\tilde{u}_i\right)$ in Equation (2) takes care of constant electrochemical potentials of electrons, ions $\{n_a, n_c\}$ and solvent molecules. r denotes the spatial coordinates.

Under thermodynamic equilibrium, minimizing the Ω with respect to n_e and ϕ, respectively, leads to the following two controlling equations,[24,25]

$$\overline{\nabla}\overline{\nabla}\overline{n}_e = \frac{20}{3}\overline{n}_e\frac{\omega}{\theta_T\omega-\theta_{XC}}\left[\frac{\partial t_{TF}}{\partial\overline{n}_e}+\frac{\partial u_X^0}{\partial\overline{n}_e}+\frac{\partial u_C^0}{\partial\overline{n}_e}-\frac{(e_0\phi+\tilde{\mu}_e)}{e_{au}}\right] + \frac{\left(\theta_T\omega-\frac{4}{3}\theta_{XC}\right)}{2\overline{n}_e(\theta_T\omega-\theta_{XC})}\left(\overline{\nabla}\overline{n}_e\right)^2, \quad (8)$$

$$-\overline{\nabla}\left[\overline{\epsilon}_{hf}\overline{\nabla}\overline{\phi}+\sum_{l=1}^{N_C}\delta(l\in S)\overline{n}_l\overline{p}_l\kappa\mathcal{L}_l\right] = \kappa\left[\left(\overline{n}_{cc}-\ \overline{n}_e\right)+\sum\nolimits_{l=1}^{N_C}\delta(l\in M)\overline{n}_l\overline{q}_l\right], \quad (9)$$

where the overbar denotes variables and operators in the dimensionless system, $\overline{\nabla}=a_0\nabla$ with a_0 (=Bohr radius) the reference length, $\overline{n}_e=n_e(a_0)^3$, $\overline{\phi}=\frac{e_0\phi}{k_BT}$ with e_0 the elementary charge. $\overline{\epsilon}_{hf}=\frac{\epsilon_{hf}}{\epsilon_0}$ with ϵ_0 the permittivity of vacuum, $\overline{p}=\frac{p}{e_0a_0}$, $\overline{q}=\frac{q}{e_0}$, and $\overline{n}_{cc}$ are the dimensionless high-frequency permittivity, dipole moment of solvent, charge of electrolyte ions, and charge density of metal cationic cores, respectively. In Equation (8), $\omega=\frac{2}{5}\pi^{\frac{5}{3}}3^{\frac{1}{3}}(\overline{n}_e)^{\frac{1}{3}}$. t_{TF} is the kinetic energy functional, u_X^0 and u_C^0 are the exchange and correlation energy functional of a homogeneous electronic system, respectively. θ_T and θ_{XC} are the gradient coefficients tuning the contribution of the "semilocal" term in kinetic energy and exchange-correlation energy, respectively. $\tilde{\mu}_e$ is the electrochemical potential of electrons. $e_{au}=27.2$ eV is the energy in atomic units. In Equation (9), $\kappa=\frac{e_0^2}{k_BT\epsilon_0a_0}$ is a scalar number derived from fundamental constants, and $\mathcal{L}_l=\coth\left(\overline{p}_l\overline{E}\right)-1/\left(\overline{p}_l\overline{E}\right)$ with $\overline{E}=\left|\nabla\overline{\phi}\right|$ being the dimensionless electric field. $\overline{n}_l\,(l=a,c,s)$ can be obtained by minimizing the Ω with respect to n_l,

$$\overline{n}_l=\frac{\Theta_l}{1+\sum_{l=1}^{N_C}\gamma_l\chi_l(\Theta_l-1)}, \quad (10)$$

where γ_l is the relative size of particles of the type l referenced to the characteristic length of referenced lattice Λ_B. χ_l $(=n_l^b/n_{max})$ is the dimensionless bulk number densities χ_l with $n_{max}=\Lambda_B{}^{-3}$. Θ_l denotes thermodynamic factors, given by,

$$\Theta_l=\exp\left(-\beta\left(\delta(l\in M)q_l\phi-\delta(l\in S)\beta^{-1}\ln\frac{\sinh(\beta p_l|\nabla\phi|)}{\beta p_l|\nabla\phi|}+w_l\right)\right). \quad (11)$$

Equations (8–11) constitute a closed set of controlling equations that allow solving for the electrostatic potential and the density profiles of electrons, solvent molecules, and ions.

2.2 | Simulation of three potential causes of ultralow PZ slopes

2.2.1 | Surface roughness

In this work, we apply the DPFT to a two-dimensional model that incorporates surface roughness. Specifically, we model rough electrode surfaces with a sinusoidal profile. This profile is characterized by two key parameters: the roughness length l_s and the roughness height h_s, as illustrated in Figure 2A. For rough electrodes, the shortest distance, defined as $d\left(\vec{r}\right)=\sqrt{(x_0-x)^2+(y_0-y)^2}$, between a particle at (x_0,y_0) and the rough surface $S(x,y)$, is used to calculate the electrode–electrolyte interaction and local permittivity.

2.2.2 | Nonspecific ion attraction

The DPFT framework describes short-range metal–solution interactions using Morse potential, as depicted in Figure 2B. Dolbhoff-Dier and Koper argued that the short-range attractive forces should be similar for both cations and anions in order to explain the ultrahigh C_{dl} at the PZC, namely, the ion adsorption is *nonspecific*.[17] We systematically vary two key parameters in Equation (7), that is, the depth of the ion potential well D_{ion} and the equilibrium distance between ions and metal surface $d_{0,ion}$, to assess how nonspecific ion attraction influences C_{dl} and the PZ slopes. In the base case, the Morse potential for ions is characterized by parameters $D_a=D_c=D_{ion}=0.04$ eV and $d_{0,ion}=4$ Å, while water molecules are described with $D_{H_2O}=0.25$ eV and $d_{0,H_2O}=2.85$ Å, inherited from a previous work.[25]

2.2.3 | Ion chemisorption with partial charge transfer

Very recently, we extended the standard DPFT framework to account for ion chemisorption, called DPFT-Chem,[27] thereby offering an improved description of electrocatalytic interfaces. The DPFT-Chem model employs an implicit treatment of ion chemisorption based on the Anderson–Newns model Hamiltonian.[49–54] Three aspects of this treatment are noted. First, chemisorbed ions are desolvated and have the radius of the bare anion, as illustrated in Figure 2C. Here, the radius of the chemisorbed anion is set as 1.4 Å. Second, charge transfer occurs between the metal surface and ions, inducing an effective partial charge on the chemisorbed ion. For a monovalent chemisorbed anion, its partial charge q_{ca} is determined using the Anderson–Newns Hamiltonian,[27]

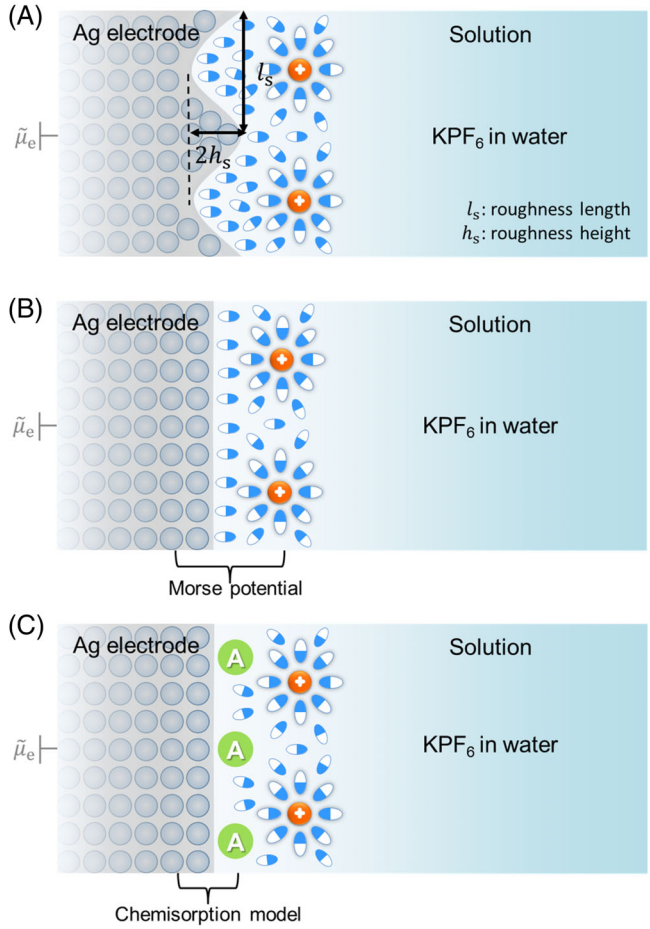

FIGURE 2 Modeling three potential causes, that is, surface roughness, nonspecific ion attraction, and ion chemisorption with partial charge transfer. (A) Double layer structure of a negatively charged, sinusoidal-shaped Ag-KPF_6 aqueous interface. Without considering specific adsorption, the Ag surface is covered by a layer of water molecules. The excess electron on Ag is balanced by solvated cations in the diffuse layer. Specifically, we consider a sinusoidal surface with two characteristic lengths, that is, the roughness length l_s and the roughness height h_s. $\tilde{\mu}_e$ is the electrochemical potential of electrons. (B) Double layer structure of a negatively charged, planar Ag(111)-KPF_6 aqueous interface. Nonspecific ion attraction is modeled using Morse potential. (C) Double layer structure of a negatively charged, planar Ag(111)-KPF_6 aqueous interface with partially charged chemisorbates (denoted A) located at the inner Helmholtz plane. The anion chemisorption is described using the Anderson–Newns model Hamiltonian approach.

$$q_{ca}\left(d\left(\vec{r}\right)\right) = -\frac{1}{2} + \frac{1}{\pi}\arctan\left(\frac{\epsilon_{ca}}{\Delta}\right), \tag{12}$$

where $\Delta = \Delta^0 \exp\left[-\kappa_\Delta\left(d\left(\vec{r}\right) - d_{cut}\right)\theta\left(d\left(\vec{r}\right) - d_{cut}\right)\right]$ is the strength of the electronic metal–anion interaction which decreases exponentially with the anion moving away from the metal surface, κ_Δ is the coefficient determining the exponential decay of Δ, d is the distance of the anion away from the metal surface, d_{cut} is the cutoff distance, and $\theta(x)$ is the Heaviside function. $\epsilon_{ca} = -\tilde{\mu}_e + \left[\epsilon^0_{ca} - \Delta_\epsilon\left(1 - \exp\left(-\kappa_\epsilon\left(d\left(\vec{r}\right) - d_{cut}\right)\theta\left(d\left(\vec{r}\right) - d_{cut}\right)\right)\right)\right]$ is the energy level of the valence orbital of the anion referenced to the Fermi level of the metal. ϵ_{ca} also changes with the distance d, characterized with a magnitude of $\Delta_\epsilon > 0$ and a coefficient of κ_ϵ. ϵ^0_{ca} is the reference value at $d = d_c$. The increase in ϵ_{ca} with decreasing d facilitates transferring the electron from the anion to the metal. Lastly, the depth of potential well, D_{ca}, for anion chemisorption is considerably larger than that for the nonspecifically adsorbed ions and varies with the electrochemical potential of electrons $\tilde{\mu}_e$.[55,56] To account for this dependency, we introduce a potential-dependent well depth defined as

$$D_{ca} = \frac{1}{k_B T}\left(D^0_{ca} + \alpha_{ca}\tilde{\mu}_e\right), \tag{13}$$

where the coefficient $\alpha_{ca} < 0$, and D^0_{ca} denotes the intercept at $\tilde{\mu}_e = 0$ eV. Note that Equation (13) does not include the electrostatic interactions, which are described separately through Equation (11). Additionally, the equilibrium distance between the chemisorbed anion and the metal surface, $d_{0,ca}$, is fixed at 2.8 Å. The remaining parameters of the Anderson–Newns Hamiltonian are listed in Table S2.

In the DPFT-Chem framework, the total surface charge σ_{tot} is the sum of the chemisorption-induced surface charge σ_{ad} and the Gouy–Chapman diffuse layer charge σ_{GC}, represented as $\sigma_{tot} = \sigma_{ad} + \sigma_{GC}$.[27] A detailed conceptual analysis of surface charge densities and differential capacitances is referred to Reference 27. Correspondingly, the total capacitance C_T is also a combination of the chemisorption capacitance C_{ad} and the C_{GC}.

2.3 | Computational details of DPFT

2.3.1 | Initial guess

In this work, we use the following initial guess for the electron density and its gradient

$$\overline{n}_e(\overline{x}) = \frac{\overline{n}^0_{cc}}{2}\mathrm{erfc}(\beta_{ini}(\overline{x} - \overline{x}_m)), \tag{14}$$

$$\overline{\nabla}\overline{n}_e(\overline{x}) = \frac{\beta_{ini}\overline{n}^0_{cc}}{\sqrt{\pi}}\exp\left(-\beta^2_{ini}(\overline{x} - \overline{x}_m)^2\right), \tag{15}$$

where $\overline{n}^0_{cc} = 4N_{Ag}\left(\frac{a_0}{a_{Ag}}\right)^3 = 0.408$ with $N_{Ag} = 47$ representing the number of all electrons of a sliver atom, and $a_{Ag} = 4.08$ Å is the lattice constant of the cubic closed-packed cell of Ag, which contains four sliver atoms. β_{ini} is the width of the transition region. Correspondingly, the initial guess for the electric potential is obtained from solving the Poisson equation $-\overline{\nabla}^2\overline{\phi} = \kappa(\overline{n}_{cc} - \overline{n}_e)$,

$$\overline{\phi}(\overline{x}) = \frac{\kappa\overline{n}^0_{cc}}{8\beta^2_{ini}}\begin{pmatrix} -4\beta^2_{ini}(\overline{x} - \overline{x}_M)^2\theta(\overline{x}_M - \overline{x}) + \left(1 + 2\beta^2_{ini}(\overline{x} - \overline{x}_M)^2\right)\mathrm{erfc}(\beta_{ini}(\overline{x} - \overline{x}_M)) \\ -2\frac{\beta_{ini}(\overline{x} - \overline{x}_M)}{\sqrt{\pi}}\exp\left(-\beta^2_{ini}(\overline{x} - \overline{x}_M)^2\right) \end{pmatrix} \tag{16}$$

and the corresponding potential gradient reads,

$$\overline{\nabla\phi}(\bar{x}) = -\frac{\kappa\bar{n}_{cc}^{0}}{2\beta_{ini}}\left(\begin{array}{c} 2\beta_{ini}(\bar{x}-\bar{x}_M)\theta(\bar{x}_M-\bar{x}) + \frac{1}{\sqrt{\pi}}\exp\left(-\beta_{ini}^2(\bar{x}-\bar{x}_M)^2\right) \\ -\beta_{ini}(\bar{x}-\bar{x}_M)\mathrm{erfc}(\beta_{ini}(\bar{x}-\bar{x}_M)) \end{array}\right). \quad (17)$$

Here, $\theta(\bar{x}_M-\bar{x})$ is a Heaviside function, which is equal to 1 when $\bar{x} < \bar{x}_M$ and zero elsewise.

2.3.2 | Boundary conditions

The ordinary differential equations (ODEs) in Equations (8) and (9) are solved with the following boundary conditions: $\overline{\nabla}\bar{n}_e = 0, \overline{\nabla\phi} = 0$ at the bulk metal; $\bar{n}_e = 0$, $\bar{\phi} = 0$ at the bulk solution. These boundary conditions ensure that the DPFT solution is independent of the position of the metal–electrolyte boundary. Interfacial distributions of electron density, solvent density, ion density, and electric potential are obtained through a self-consistent solution of the coupled equations. Additionally, the electric potential in the metal phase, E_M, is not directly imposed in the boundary conditions. Instead, constant-potential simulations are achieved by adjusting the electrochemical potential of electrons, $\tilde{\mu}_e$, in Equation (8), which effectively corresponds to varying E_M up to an additive constant of e_0,

$$\tilde{\mu}_e = \mu_e - e_0 E_M, \quad (18)$$

where $\mu_e = \frac{\partial t_{TF}}{\partial n_e} + \frac{\partial u_X^0}{\partial n_e} + \frac{\partial u_c^0}{\partial n_e}$ is the chemical potential of electrons with a uniform density.

2.3.3 | Implementation

All DPFT simulations are performed in COMSOL Multiphysics. The two controlling equations, Equations (8) and (9), are implemented as a coefficient-form ODE. All parameters used in the DPFT simulations are summarized in Tables S1.

2.4 | Calculation of C_{dl} and C_T

The In absence of chemisorption, C_{dl} is calculated as

$$C_{dl} = \frac{\partial\sigma_{free}}{\partial E_M} = -e_0\frac{\partial\sigma_{free}}{\partial\tilde{\mu}_e}, \quad (19)$$

where σ_{free} is the free surface charge density. The σ_{free} of the EDL is calculated from,

$$\sigma_{free} = -\frac{e_0}{a_0^2}\int d\bar{x}(\bar{n}_c - \bar{n}_a) = -\frac{e_0}{a_0^2}\int d\bar{x}(\bar{n}_e - \bar{n}_{cc}), \quad (20)$$

where the second equality in Equation (20) reflects the fact that the whole EDL is electroneutral, and the factor e_0/a_0^2 is for dimensional balance. The substitution of Equation (20) into Equation (19) gives the following equation for calculating the C_{dl}:

$$C_{dl} = \frac{e_0^2\partial}{a_0^2\partial\tilde{\mu}_e}\int d\bar{x}(\bar{n}_c - \bar{n}_a) = \frac{e_0^2\partial}{a_0^2\partial\tilde{\mu}_e}\int d\bar{x}(\bar{n}_e - \bar{n}_{cc}), \quad (21)$$

The C_T is defined as

$$C_T = \frac{\partial\sigma_{tot}}{\partial E_M} = -e_0\frac{\partial\sigma_{tot}}{\partial\tilde{\mu}_e}, \quad (22)$$

where σ_{tot} is the total surface charge density. It can be expressed as,

$$\sigma_{tot} = -\frac{e_0}{a_0^2}\int d\bar{x}(\bar{n}_c - \bar{n}_a - \bar{n}_{a,A}), \quad (23)$$

where $\bar{n}_{a,A}$ denotes the density of chemisorbed anions. In absence of chemisorption, *i.e.*, $\bar{n}_{a,A} = 0$, σ_{tot} reduces to σ_{free}. Substituting Equation (23) into Equation (22) gives the following expression for C_T:

$$C_T = \frac{e_0^2\partial}{a_0^2\partial\tilde{\mu}_e}\int d\bar{x}(\bar{n}_c - \bar{n}_a - \bar{n}_{a,A}), \quad (24)$$

Similarly, in absence of chemisorption, C_T reduces to C_{dl}. Throughout this paper and in all figures, we use C_T uniformly and it is understood that C_T is equal to C_{dl} in absence of chemisorption.

It is also worth noting that for a two-dimensional rough interface, the projected surface area (flat cross-section area) A_{proj} is utilized to calculate C_T, in order to be consistent with previous studies.[56,57]

2.5 | Calculation of the PZ slope

The PZ slope is determined from the linear relationship obtained by plotting the inverse of the measured total capacitance C_T against the inverse of C_{GC}, which is given by,[17,51,57,58]

$$C_{GC} = \frac{\varepsilon_r\epsilon_0}{\lambda_D}, \quad (25)$$

where ε_r is the relative permittivity of solvent, λ_D is the Debye length. By collecting data at various electrolyte concentrations, the PZ plot is constructed by plotting $1/C_T$ vs. $1/C_{GC}$, and the linear slope obtained from this plot is defined as the PZ slope.

3 | RESULTS AND DISCUSSIONS

3.1 | Verification of the DPFT models for Parsons–Zobel plots

The accuracy of the DPFT model is first examined using the PZ plot of planar Ag(111)-KPF_6 aqueous interface. Valette systematically measured the C_{dl} curves of planar Ag(111) electrode in x mM KPF_6 ($x = 5$, 10, 20, 40, and 100) aqueous solutions. Valette's data are corrected using the roughness factor of 1.08 suggested by Valette himself, which are used as the experimental benchmark.[13]

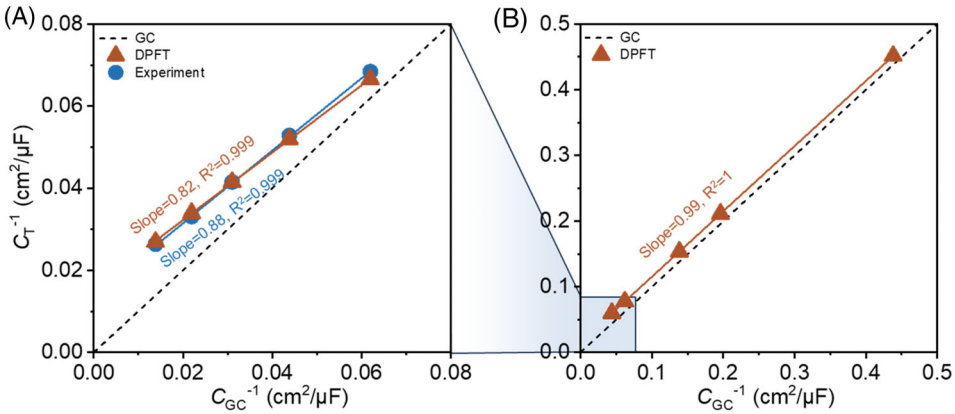

FIGURE 3 Parsons–Zobel (PZ) plots for the planar Ag-KPF_6 aqueous interfaces at the potential of zero charge (PZC). (A) Comparison between 2D density-potential functional theory (DPFT) model and experimental results of the PZ plots at the PZC for the Ag(111)-KPF_6 aqueous interface. Experimental data were taken from the work of Valette,[13] where the total capacitance C_T, which is equal to C_{dl} in this case, curves at five concentrations, 5, 10, 20, 40, and 100 mM, were measured at 25 ± 2°C. The experimental data have been corrected using the roughness factor of 1.08 determined by Valette himself. (B) PZ plots for Ag(111)-KPF_6 aqueous interface using DPFT model at the PZC at five small concentrations (0.1, 0.5, 1, 5, and 10 mM). A 45° line going through the coordinate origin is plotted for "guides to eye." The slopes are obtained by linear fitting to the calculated data.

As shown in Figure 3A, the experimental PZ slope is 0.88 at the PZC, with a sizeable deviation from the theoretical value of 1. We note that all experimental data points lie above the 45° line due to the contribution of C_H. The DPFT model gives a PZ slope of 0.82 at the PZC, which agrees reasonably with the experimental value. The exceptionally high correlation coefficient ($R^2 = 0.999$) from the linear fitting of the data indicates that C_H remains independent of ion concentration. Notably, in the absence of surface roughness or chemisorption, the DPFT model gives a PZ slope smaller than 1. This deviation from unity is attributed to the point charge assumption of the Gouy–Chapman model, which is valid only in the dilute electrolyte limit.[18]

To lessen the importance of ion size effects, we extend the DPFT model calculations to very dilute electrolyte solutions (0.1, 0.5, 1, 5, and 10 mM). We would then expect that the PZ plot will approach the 45° line, yielding a slope of approximately 1. Our hypothesis is supported by the model results displayed in Figure 3B. In the concentration range between 0.1 and 10 mM, the PZ plot for the planar Ag(111)-KPF_6 aqueous interface exhibits a fitted slope of 0.99, with $R^2 \approx 1$. It is worth noting that simulating a 10 mM aqueous electrolyte requires accounting for at least 5560 water molecules given $n_{water} = 55.6$ M. This number of water molecules would present a tremendous computational burden for Kohn–Sham DFT-based approaches. In the remainder of this work, all subsequent calculations of the PZ slope are performed at these five concentrations.

3.2 | Effects of surface roughness on Parsons–Zobel slopes

Having demonstrated the accuracy of the DPFT model for planar electrodes, we examine the effects of surface roughness, ion attraction, and ion chemisorption on the PZ slope separately. Firstly, as regards the surface roughness, there are two computational methods in the literature for determining the PZ slope: surface area correction (SAC)[16,59] and perturbation theory (PT).[57,58] The SAC method defines the PZ slope as the ratio of the projected surface area A_{proj} to the real surface area A_{real}.[59] While this method provides an initial framework to account for roughness, it is insufficient to explain why the Ag(111) electrode exhibits different PZ slopes in various electrolytes, as shown in Figure S1. The SAC method simplifies the roughness effects by ignoring all interplay between surface irregularities and the electrostatic interactions characterized by λ_D, and the electronic interactions characterized by the Thomas–Fermi screening length λ_{TF}.[57] These omissions might cause the method to fall short of capturing the complexity of roughness effects on C_{dl}.

To account for the effects of electrostatic interaction on the PZ slopes, Daikhin et al.[57] employed PT, which treats surface roughness as an perturbation of the electrostatic field. By applying PT to both linear[57] and nonlinear[58] Poisson–Boltzmann (PB) models, they derived analytical expressions for the effects of surface roughness on C_{dl} for various surface geometries, including Euclidean surfaces of sinusoidal corrugation and random Gaussian roughness, as well as non-Euclidean self-affine fractal surfaces. However, it is important to note that PT is only applicable when the characteristic length of surface roughness is smaller than the Debye length, which is approximately 1 nm for an electrolyte concentration of 100 mM and at room temperature.[57,58] At such small length scales, metal electronic effects and short-range interactions between the metal and solution cannot be neglected. In comparison, the DPFT model accounts for these hybrid quantum-classical factors in a unified framework that is cheap enough, thus opening the door to simulating EDLs with nanoscale roughness.

To assess the description of surface roughness effects in different methods, we calculate PZ plots using DPFT, SAC, and PT methods for sinusoidal-shaped Ag-solution interfaces. Two characteristic lengths—

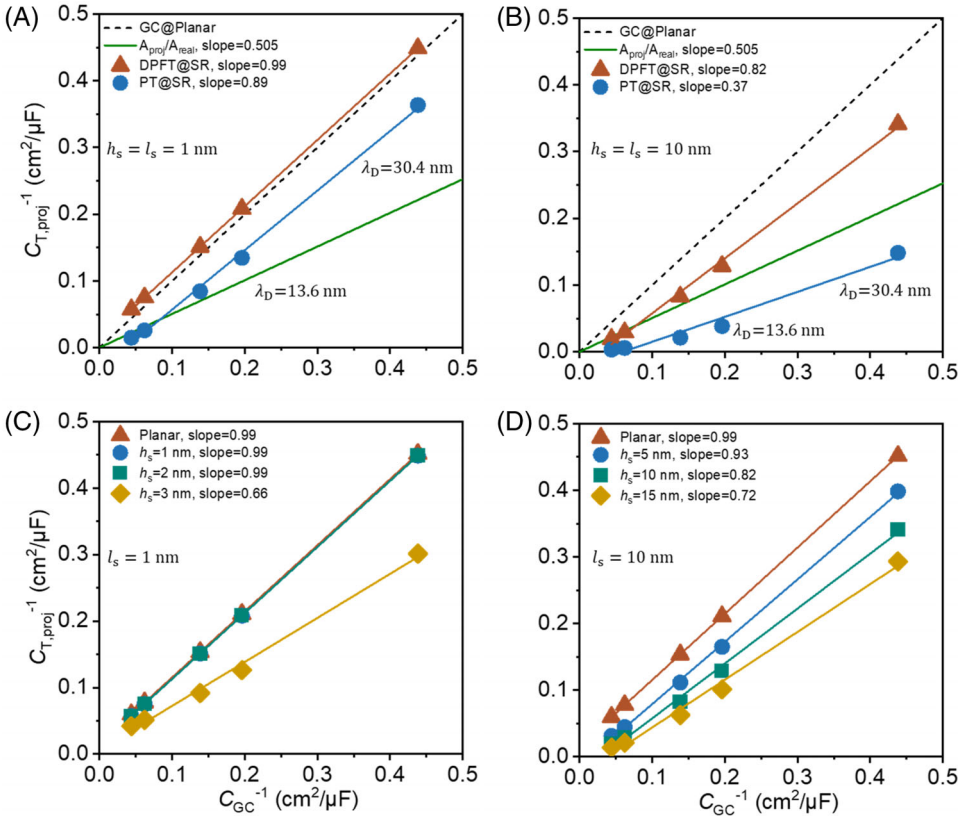

FIGURE 4 Parsons–Zobel (PZ) plots for the planar surface and surfaces with various roughness at the potential of zero charge (PZC). Comparison of PZ slopes for sinusoidal-shaped Ag-solution interfaces with (A) $h_s = l_s = 1$ nm and (B) $h_s = l_s = 10$ nm using DPFT, surface area correction (SAC), and perturbation theory (PT) at the PZC. The total capacitance C_T, which is equal to C_{dl} in this case, is calculated at five dilute concentrations (0.1, 0.5, 1, 5, and 10 mM). A 45° line going through the coordinate origin is plotted for "guides to eye." PZ plots for sinusoidal-shaped Ag-solution interfaces with (C) $l_s = 1$ nm and $h_s = 1, 2, 3$ nm and (D) $l_s = 10$ nm and $h_s = 5, 10, 15$ nm at the PZC. The C_T are calculated at five dilute concentrations (0.1, 0.5, 1, 5, and 10 mM). The slopes are obtained by linear fitting to the calculated data at the five concentrations.

the roughness length l_s and the roughness height h_s—are varied in this comparison, as shown in Figure 2A. Figure 4A,B present the results for the case with $l_s = h_s = 1$ nm and $l_s = h_s = 10$ nm, respectively. Two reference straight lines are added, including one calculated using the GC model on a planar electrode (black solid line), and the other calculated using the SAC method (green solid line). The latter gives a PZ slope of 0.505 for cases with $l_s = h_s$.

In the case of $l_s = h_s = 1$ nm, the DPFT model yields a PZ slope of 0.99, which is much higher than the value of 0.505 given by the SAC method. This nearly-unit slope can be explained by the hydrophilicity of the Ag(111) surface. The DPFT model assumes that the binding energy of H_2O (0.25 eV) is larger than that of solvated ions (0.04 eV).[25,60] As a result, water molecules preferentially occupy the valleys of the rough surface, effectively "flattening" the interface.[61] This flattening effect reduces the roughness factor, leading to a PZ slope of 0.99. In comparison, the PT model predicts a lower PZ slope of 0.89. This discrepancy arises from the fact that PT only considers electrostatic interactions on the electrolyte side, neglecting short-range metal–solution interactions and metal electronic effects.

As the roughness scale increases, the limitations of PT approach become more pronounced. For instance, for the case of $l_s = h_s = 10$ nm, PT predicts a significantly reduced PZ slope of 0.37, as shown in Figure 4B, which is even lower than the value given by the SAC method. Furthermore, the PZ slope is scale-dependent. Specifically, the PZ slope is different for different roughness scales even when the ratio of l_s to h_s remains constant. The scale dependency suggests that simple geometric corrections like the SAC method are inadequate to capture the full landscape of surface roughness effects on PZ slopes.

To further explore the roughness effects on the PZ slope, we employ the DPFT model to systematically calculate PZ plots as a function of one characteristic roughness length while fixing the other. Figure 4C illustrates PZ plots for $l_s = 1$ nm and varying roughness heights $h_s = 1, 2, 3$ nm. At smaller roughness values ($h_s = 1, 2$ nm), the PZ plot of these rough surfaces coincides with that of the planar surface, indicating a negligible roughness effect due to the flattening effect of water.[61] However, as h_s increases to 3 nm, the PZ plot has a slope of 0.66, because $h_s = 3$ nm falls within the range of electrostatic screening lengths for the five concentrations of solution (Debye lengths are 3.0, 4.3, 9.6, 13.6, and 30.4 nm, respectively). Figure 4D shows PZ plots for $l_s = 10$ nm with varying h_s (= 5, 10, 15 nm). PZ slopes are 0.93, 0.82, and 0.72, respectively, as h_s increases.

Recalling the experimental data shown in Figure 1A, while surface roughness will reduce the PZ slope, it alone cannot account for the ultralow slopes observed in experimental data for Au(111) and Pt(111). Additional factors, such as ion attraction and ion chemisorption, have been introduced to understand the observed deviations from classical theory, which are to be explored further in subsequent sections.

3.3 | Effects of ion attraction on Parsons–Zobel slopes

Surface roughness alone cannot account for the ultralow PZ slopes observed in experiments conducted with meticulously prepared single-crystal electrodes. Consequently, we turn our attention to other potential factors including ion attraction and ion chemisorption, both of which have been shown to significantly influence PZ slopes in previous works.[17,18] To fully grasp their effects, a more detailed and systematic investigation is conducted within the DPFT framework.

We begin by analyzing a simple scenario where the ion attraction effects are singled out by explicitly excluding any charge transfer between metal surface and ions. Figures S2a and 5B display computed PZ plots for various D_{ion} values, ranging from 0.14 to 0.35 eV. When D_{ion} is smaller than the ion-water interaction energy of 0.25 eV, the PZ plots become nonlinear. This deviation results in PZ slopes greater than 1, as depicted in Figure S2a. As D_{ion} increases beyond D_{H_2O}, as shown in Figure 5A, the PZ slopes decrease down to 0.468, 0.103, and 0.03 for D_{ion} of 0.25, 0.30, and 0.35 eV, respectively. These slopes are closer to experimental results for Au(111) and Pt(111) surfaces, suggesting that significant reductions in the PZ slope occur only when ion–metal interactions are comparable to or even stronger than metal–solvent interactions. This does not mean that the metal surface is in direct contact with bare ions because the ions are dressed in a solvation shell. Determining the exact value of D_{ion} between the metal surface and the solvated ion through *ab initio* calculations and experiments is challenging due to the changes in the solvation shell as the ion approaches the surface. However, it is largely agreed that the electrostatic shielding effect of the solvation shell significantly

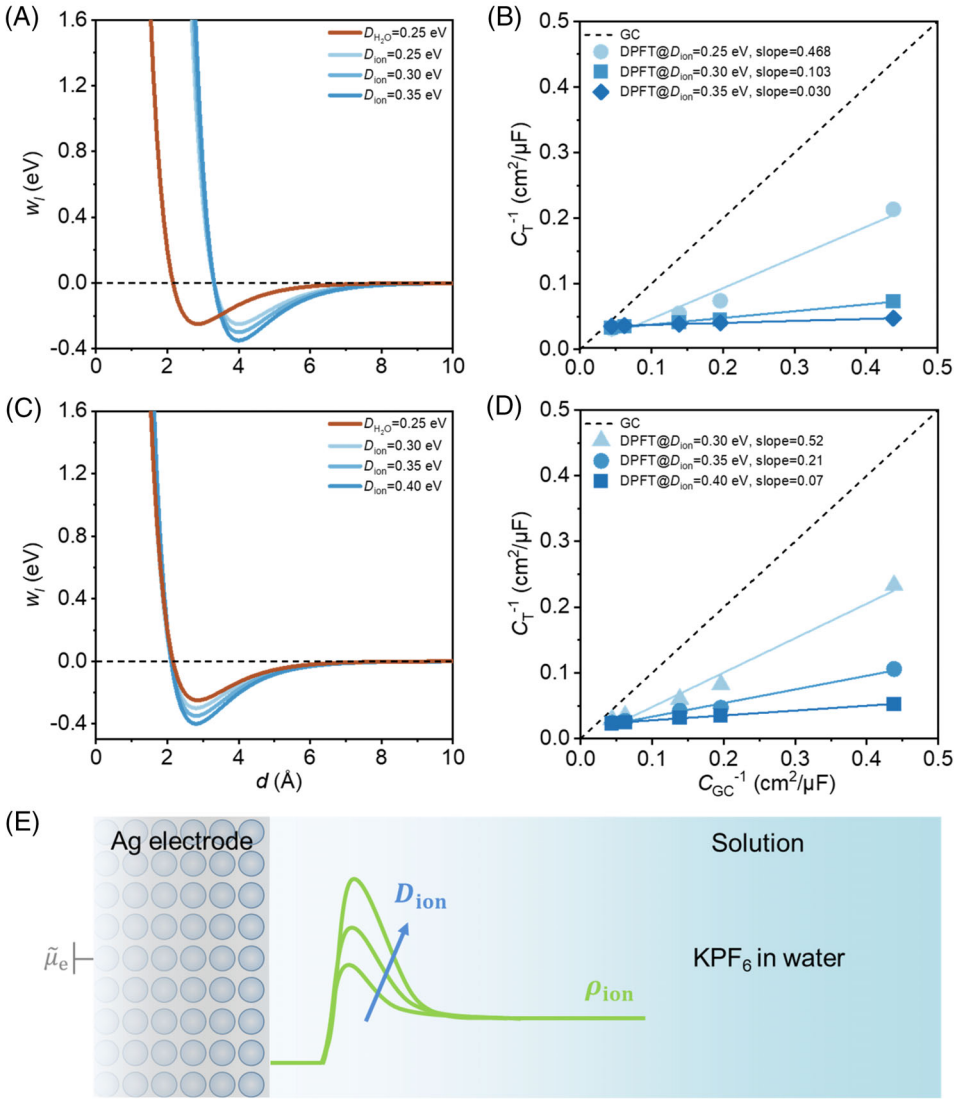

FIGURE 5 Impact of ion attraction strengths on Parsons–Zobel (PZ) plots. (A) Morse potential profiles w_I for ions with varying attraction strengths $D_a = D_c = D_{ion} = 0.25, 0.30, 0.35$ eV and $d_{0,ion} = 4$ Å, as well as for water with $D_{H_2O} = 0.25$ eV and $d_{0,H_2O} = 2.85$ Å. (B) PZ slopes for planar Ag-solution interfaces with varying attraction strengths $D_{ion} = 0.25, 0.30, 0.35$ eV at the potential of zero charge (PZC). (C) Morse potential profiles w_I for ions with varying attraction strengths $D_a = D_c = D_{ion} = 0.30, 0.35, 0.40$ eV and $d_{0,ion} = 2.8$ Å, as well as for water with $D_{H_2O} = 0.25$ eV and $d_{0,H_2O} = 2.85$ Å. (D) PZ slopes for planar Ag-solution interfaces with $D_{ion} = 0.30, 0.35, 0.40$ eV and $d_{0,ion} = 2.8$ Å at the PZC. The total differential capacitance C_T are calculated at five dilute concentrations (0.1, 0.5, 1, 5, and 10 mM). The slopes in (B) and (D) are obtained by linear fitting to the calculated data at the five concentrations. The PZ plot of Gouy–Chapman (GC) in (B) is located at the 45° line and is plotted for "guides to eye." (E) Schematic of the effect of D_{ion} on the local ion concentration distribution ρ_{ion}. As D_{ion} gets larger, the ρ_{ion} near the metal surface increases.

weakens the electrostatic interaction between the metal and solvated ions.[62] As a result, the D_{ion} is predominantly governed by van der Waals forces, with a magnitude of approximately 0.05 eV.[63–66] This indicates that the value of D_{ion} required to achieve a ultrasmall PZ slope, is highly unrealistic.

Figure S3 shows DPFT-calculated C_T for several values of D_{ion}. Interestingly, the change in Morse potential w_l does not affect the PZC,[26] hence, the PZC for all C_T curves remains at $\tilde{\mu}_e = -3.86$ eV. At this PZC, the C_T curves transition from camel-shaped to bell-shaped curves with increasing D_{ion}, indicating a rise in C_T due to stronger ion attraction. This increase in C_T is attributed to the elevated local ion concentration near the surface, as schematically depicted in Figure 5E.

Next, we explore the effect of varying the equilibrium distance $d_{0,ion}$ between ions and metal surface. Figure 5D presents the PZ slopes for $d_{0,ion} = 2.8$ Å, which is slightly lower than the distance between water molecules and metal surface, $d_{0,H_2O} = 2.85$ Å. The corresponding Morse potential profiles with varying D_{ion} are depicted in Figure 5C. Figures S2b and 5D show PZ plots for D_{ion} values from 0.04 to 0.4 eV. Given the proximity of $d_{0,ion}$ and d_{0,H_2O}, a larger ion attraction potential is necessary to expel water molecules from the surface and reduce the PZ slope. This observation is critical, as it suggests that only under such conditions can the experimentally observed ultralow PZ slopes for Au(111) and Pt(111) surfaces be reproduced.

A closer examination of the C_T curves in Figures S3 and S4 reveals that the C_T at high electrolyte concentrations varies only slightly at the PZC as the ion attraction potential increases. The reduction in PZ slopes at the PZC correlates with a transition in the C_T curves from hump-shaped to dumbbell-shaped at lower concentrations. While these findings provide insights into how ion attraction influences the PZ slope, a direct comparison of the experimental and calculated C_T values reveal a significant discrepancy: the calculated C_T values for both cases are substantially smaller than those observed experimentally. For example, in experiments involving Pt(111) electrode in 0.1–5 mM $NaClO_4$, $LiClO_4$, $CsClO_4$, $NaCH_3SO_3$, and LiF electrolytes, C_{dl} ranges from 50 to 120 μF/cm^2 at the PZC,[14,21] whereas our calculated C_T at 10 mM is only around 30 μF/cm^2 at the PZC. Therefore, while ion attraction contributes to the ultralow PZ slope, it cannot fully explain experimental observations. The discrepancy

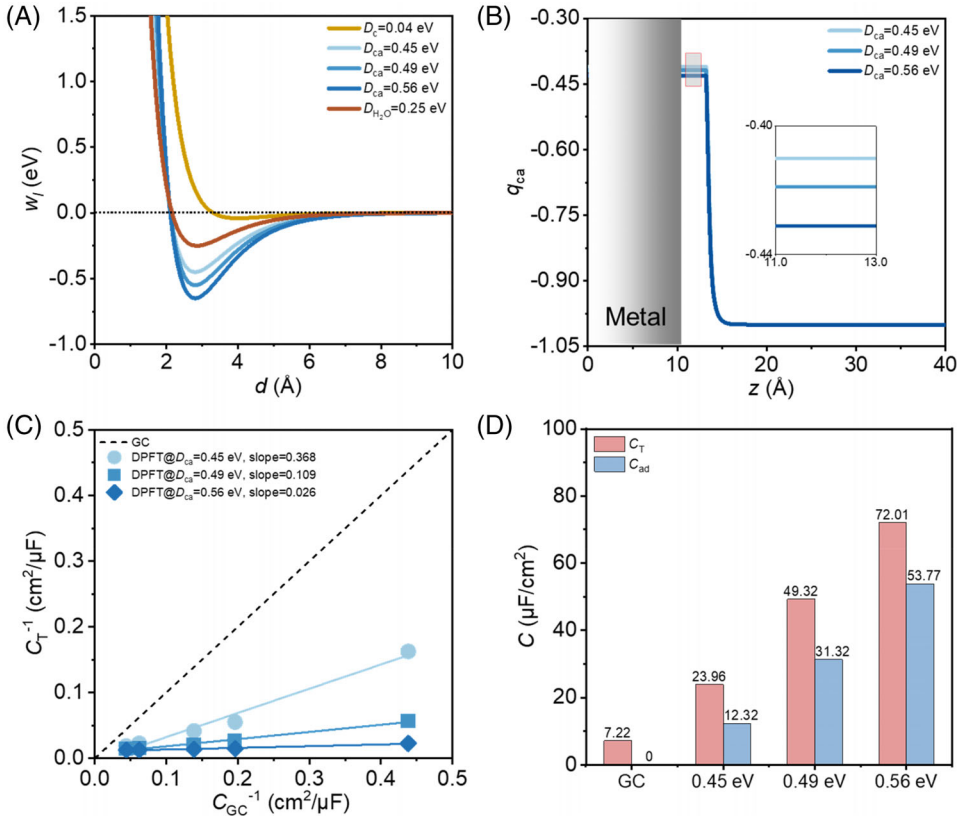

FIGURE 6 Impact of ion chemisorption strengths on Parsons–Zobel (PZ) plots. (A) Morse potential profiles w_l for cation with $D_c = 0.04$ eV and $d_{0,c} = 4$ Å, and for chemisorption anion with varying adsorption strengths $D_{ca} = 0.45, 0.49, 0.56$ eV and $d_{0,ca} = 2.8$ Å at the potential of zero charge (PZC), as well as for water with $D_{H_2O} = 0.25$ eV and $d_{0,H_2O} = 2.85$ Å. (B) The partial charge on the chemisorption anion q_{ca} as a function of its distance with varying adsorption strengths $D_{ca} = 0.45, 0.49, 0.56$ eV at the PZC. (C) PZ slopes of planar Ag-solution interfaces for chemisorption anion with varying adsorption strengths $D_{ca} = 0.45, 0.49, 0.56$ eV at the PZC. The total differential capacitance C_T are calculated at five dilute concentrations (0.1, 0.5, 1, 5, and 10 mM). The slopes are obtained by linear fitting to the calculated data at the five concentrations. The Parsons–Zobel plots of Gouy–Chapman (GC) is located at the 45° line and is plotted for "guides to eye." (D) Relative contributions of the chemisorption capacitance C_{ad} to the C_T at adsorption energies of $D_{ca} = 0.45, 0.49, 0.56$ eV at the PZC.

between calculated and measured C_T values suggests that other factors, beyond non-specific ion attraction, are at play. One of these factors is the partial charge transfer between the adsorbed ion and the metal surface, which is to be examined in the next section with a modified DPFT model.

3.4 | Effects of ion chemisorption on Parsons–Zobel slopes

We continue to examine the influence of ion chemisorption on the PZ slope using the DPFT-Chem model. Figure 6A illustrates the potential energy profiles for cations, chemisorbed anions, and solvent molecules. We vary the potential well depth D_{ca} at the PZC to 0.45, 0.49, and 0.56 eV. The corresponding charge distributions q_{ca} are depicted in Figure 6B, where q_{ca} transitions from -1 in the region of $d > 5$ Å to -0.42, -0.42, and -0.43, respectively, for $D_{ca} = 0.45, 0.49, 0.56$ eV at $d < 3$ Å. This indicates a partial charge transfer from the chemisorbed anion to the surface, which plays a crucial role in modifying the surface charges and differential capacitances. By adjusting the Morse potential well depth to 0.45, 0.49, and 0.56 eV, the DPFT-Chem model predicts PZ slopes of 0.368, 0.109, and 0.026, respectively, as illustrated in Figure 6C.

Figure S5 presents C_T curves at the PZC for different D_{ca}. C_{dl} ranges from 50 to 80 μF/cm^2 at the PZC, which closely aligns with experimental data.[14,21] Figure 6D displays the C_T and C_{ad} as a function of D_{ca}. As the chemisorption energy increases, the contribution of C_{ad} to C_T becomes more pronounced, indicating that chemisorption dominates the C_T in the presence of the chemisorption of ions.

To validate these results, we conduct additional calculations where charge transfer between anion and surface is excluded, namely, treating anions as physically adsorbed species. All other parameters remained identical to those used in Figure 6C. The resulting PZ plots are shown in Figure S6, where the PZ slopes are notably higher compared to those in Figure 6C. Additionally, as portrayed in Figure S7, the calculated C_T at the PZC is around 40 μF/cm^2 at 10 mM, with only minor variations as the potential well depth increases. This stark contrast underscores the critical role of chemisorption in explaining ultralow PZ slopes and ultrahigh capacitances. Without chemisorption, the PZ slopes and capacitance values deviate significantly from experimental observations, highlighting the limitations of ion attraction-based models. Recalling the independence of ultralow PZ slopes from the specific type of electrolyte ion, we conjecture that the underlying origin is dictated not by the unique adsorption properties of individual ions, but instead by the chemisorption of a common species. As for Pt, hydroxide ions (OH^-), formed via water decomposition, emerge as the most plausible candidate, as previously discussed in Reference 67. It has been recently showed that OH adsorption on Pt can occur on step sites at an electrode potential much negative of that on terrace sites.[68,69] Since step sites are inevitable even in real-world Pt(111), OH adsorption on Pt step sites contributing to ultrahigh C_{dl} and ultralow PZ slopes is a reasonable conjecture.

4 | CONCLUSIONS

In this study, we systematically investigated three potential mechanisms—surface roughness, nonspecific ion attraction, and ion chemisorption—to elucidate the origins of ultrahigh double layer capacitance and ultralow Parsons–Zobel (PZ) slopes at metal–solution interfaces. Using a unified density-potential functional theory (DPFT) framework, we first examined the effects of surface roughness. Our results indicate that although roughness can slightly modify the effective interfacial area, its impact is largely mitigated by the structuring of interfacial water, which tends to "flatten" the nanoscale topography. Consequently, surface roughness alone is unable to reproduce the pronounced decrease in the PZ slope observed experimentally.

Next, we explored nonspecific ion attraction as a mechanism to enhance local ion concentration. While our simulations showed that strengthening ion–metal interactions can reduce the PZ slope, the required adsorption parameters are unrealistic when compared with atomistic simulations, and the resultant double layer capacitance remains substantially lower than experimental values.

In contrast, by integrating the Anderson–Newns model Hamiltonian into our DPFT framework, we demonstrated that ion chemisorption with partial charge transfer can concurrently account for the ultrahigh capacitance and ultralow PZ slopes observed in systems such as Au and Pt. This mechanism effectively alters the local charge distribution at the interface, reconciling theoretical predictions with experimental data.

Overall, our findings establish that ion chemisorption is the dominant factor governing the interfacial behavior, providing a robust theoretical foundation that bridges fundamental electrochemical phenomena with practical applications. These insights are critical for the rational design of next-generation electrocatalytic and energy storage systems, addressing longstanding challenges in the field of chemical engineering. We note, however, that the present DPFT framework does not account for dipolar overscreening effects arising from nonlinear solvent polarization, which may become significant at low electrode polarizations.

SUPPORTING INFORMATION

PZ plots for Ag(111)-KPF_6, Ag(111)-NaF, and Ag(111)-$KClO_4$ at the PZC obtained in experiments; PZ plots for planar Ag-solution interfaces with D_{ion} at the PZC; The DPFT-calculated C_T for planar Ag-solution interfaces with different values of D_{ion}, D_a and D_{ca}; DPFT model parameters; Anderson–Newns Hamiltonian model parameters.

AUTHOR CONTRIBUTIONS

Weiqiang Tang: conceptualization, data curation, funding acquisition, investigation, methodology, validation, visualization, writing—original draft, writing—review and editing. **Shuangliang Zhao**: resources, supervision, writing—review and editing. **Michael Eikerling**: resources, project administration, supervision, writing—review and editing. **Jun Huang**: conceptualization, funding acquisition, methodology, project administration, resources, supervision, writing—review and editing.

ACKNOWLEDGMENTS

This project is supported by the Initiative and Networking Fund of the Helmholtz Association (No. VH-NG-1709) and European Research Council (ERC) Starting Grant (MESO-CAT, Grant agreement No. 101163405). Weiqiang Tang also acknowledges the financial support from the National Natural Science Foundation of China (No. 22108070) and the Young Elite Scientists Sponsorship Program by CAST (No. 2022QNRC001). We are grateful to Mr. Yufan Zhang for helpful discussions. Open Access funding enabled and organized by Projekt DEAL.

CONFLICT OF INTEREST STATEMENT

The authors declare no conflicts of interest.

DATA AVAILABILITY STATEMENT

The data that support the findings of this study are available from the corresponding author upon reasonable request. The numerical data presented in Figures 1, 3–6, and S1–S7 are available in the form of Excel sheets.

ORCID

Weiqiang Tang https://orcid.org/0000-0002-7726-4130

REFERENCES

1. Zhu X, Huang J, Eikerling M. Hierarchical modeling of the local reaction environment in electrocatalysis. *Acc Chem Res*. 2024;57(15):2080-2092.
2. Tao H, Lian C, Jiang H, Li C, Liu H, van Roij R. Enhancing electrocatalytic N2 reduction via tailoring the electric double layers. *AIChE J*. 2022;68(3):e17549.
3. Lin YJ, Chen CC. Modeling salt adsorption in electrical double layer for capacitive deionization. *AIChE J*. 2023;69(5):e18018.
4. Sundararaman R, Schwarz K. Solvent effects determine the sign of the charges of maximum entropy and capacitance at silver electrodes. *J Chem Phys*. 2023;158(12):121102.
5. Li P, Jiao Y, Huang J, Chen S. Electric double layer effects in electrocatalysis: insights from *ab initio* simulation and hierarchical continuum modeling. *JACS Au*. 2023;3(10):2640-2659.
6. Shin S-J, Kim DH, Bae G, et al. On the importance of the electric double layer structure in aqueous electrocatalysis. *Nat Commun*. 2022;13(1):174.
7. Gouy M. Sur la constitution de la charge électrique à la surface d'un électrolyte. *J Phys Theor Appl*. 1910;9(1):457-468.
8. Chapman DL. LI. A contribution to the theory of electrocapillarity. *Lond Edinb Dubl Philos Mag J Sci*. 1913;25(148):475-481.
9. Stern O. Zur theorie der elektrolytischen doppelschicht. *Z Elektrochem Angew Phys Chem*. 1924;30(21–22):508-516.
10. Grahame DC. The electrical double layer and the theory of electrocapillarity. *Chem Rev*. 1947;41(3):441-501.
11. Parsons R, Zobel FGR. The interphase between mercury and aqueous sodium dihydrogen phosphate. *J Electroanal Chem (1959)*. 1965;9(5):333-348.
12. Grahame DC. Differential capacity of mercury in aqueous sodium fluoride solutions. I. Effect of concentration at 25°. *J Am Chem Soc*. 1954;76(19):4819-4823.
13. Valette G. Double layer on silver single crystal electrodes in contact with electrolytes having anions which are slightly specifically adsorbed: part III. The (111) face. *J Electroanal Chem Interfacial Electrochem*. 1989;269(1):191-203.
14. Ojha K, Arulmozhi N, Aranzales D, Koper MT. Double layer at the Pt (111)–aqueous electrolyte interface: potential of zero charge and anomalous Gouy–Chapman screening. *Angew Chem*. 2020;132(2):721-725.
15. Hamelin A, Foresti ML, Guidelli R. Test of the Gouy–Chapman theory at a (111) silver single-crystal electrode. *J Electroanal Chem*. 1993;346(1–2):251-259.
16. Foresti ML, Guidelli R, Hamelin A. A model for the effect of roughness of single-crystal electrodes on Parsons–Zobel plots. *J Electroanal Chem*. 1993;346(1–2):73-83.
17. Doblhoff-Dier K, Koper MT. Modeling the Gouy–Chapman diffuse capacitance with attractive ion–surface interaction. *J Phys Chem C*. 2021;125(30):16664-16673.
18. Schmickler W. The effect of weak adsorption on the double layer capacitance. *ChemElectroChem*. 2021;8(22):4218-4222.
19. Schmickler W, Henderson D, Hurwitz HD. Ionic adsorption at low concentrations. *Z Phys Chem*. 1988;160(1–2):191-198.
20. Kornyshev AA, Spohr E, Vorotyntsev MA. Electrochemical interfaces: At the border line. *Encyclopedia of Electrochemistry*. Wiley Online Library; 2007.
21. Ojha K, Doblhoff-Dier K, Koper MT. Double-layer structure of the Pt (111)-aqueous electrolyte interface. *Proc Natl Acad Sci*. 2022;119(3):e2116016119.
22. Huang J, Li P, Chen S. Potential of zero charge and surface charging relation of metal–solution interphases from a constant-potential Jellium–Poisson–Boltzmann model. *Phys Rev B*. 2020;101(12):125422.
23. Huang J, Chen S, Eikerling M. Grand-canonical model of electrochemical double layers from a hybrid density–potential functional. *J Chem Theory Comput*. 2021;17(4):2417-2430.
24. Huang J. Hybrid density-potential functional theory of electric double layers. *Electrochim Acta*. 2021;389:138720.
25. Huang J. Density-potential functional theory of electrochemical double layers: calibration on the Ag(111)-KPF_6 system and parametric analysis. *J Chem Theory Comput*. 2023;19(3):1003-1013.
26. Tang W, Zhao S, Huang J. Origin of solvent dependency of the potential of zero charge. *JACS Au*. 2023;3(12):3381-3390.
27. Huang J, Domínguez-Flores F, Melander M. Variants of surface charges and capacitances in electrocatalysis: insights from density-potential functional theory embedded with an implicit chemisorption model. *PRX Energy*. 2024;3(4):043008.
28. Hedley JG, Berthoumieux H, Kornyshev AA. The dramatic effect of water structure on hydration forces and the electrical double layer. *J Phys Chem C*. 2023;127(18):8429-8447.
29. Kohn W, Sham LJ. Self-consistent equations including exchange and correlation effects. *Phys Rev*. 1965;140(4A):A1133-A1138.
30. Lundqvist S, March NH. *Theory of the Inhomogeneous Electron Gas*. Springer Science & Business Media; 2013.
31. Thomas LH. The calculation of atomic fields. *Math Proc Camb Phil Soc*. 1927;23(5):542-548.
32. Fermi E. Eine statistische Methode zur Bestimmung einiger Eigenschaften des Atoms und ihre Anwendung auf die Theorie des periodischen Systems der Elemente. *Z Phys*. 1928;48(1–2):73-79.
33. Perdew JP, Kurth S. Density functionals for non-relativistic coulomb systems in the new century. In: Fiolhais C, Nogueira F, Marques MAL, eds. *A Primer in Density Functional Theory*. Springer Berlin Heidelberg; 2003:1-55.
34. Lue L. A variational field theory for solutions of charged, rigid particles. *Fluid Phase Equilib*. 2006;241(1):236-247.
35. Hubbard J. Calculation of partition functions. *Phys Rev Lett*. 1959;3(2):77-78.
36. Caillol J-M, Patsahan O, Mryglod I. Statistical field theory for simple fluids: the collective variables representation. *Phys A Stat Mech Appl*. 2006;368(2):326-344.
37. Budkov YA. Statistical field theory of ion–molecular solutions. *Phys Chem Chem Phys*. 2020;22(26):14756-14772.
38. Budkov YA. Nonlocal statistical field theory of dipolar particles in electrolyte solutions. *J Phys Condens Matter*. 2018;30(34):344001.
39. Agrawal NR, Wang R. Non-monotonic salt concentration dependence of inverted electrokinetic flow. *AIChE J*. 2023;69(12):e18269.

40. Tang W, Cai C, Zhao S, Liu H. Development of reaction density functional theory and its application to glycine tautomerization reaction in aqueous solution. *J Phys Chem C*. 2018;122(36):20745-20754.
41. Bikerman J. XXXIX. Structure and capacity of electrical double layer. *Lond Edinb Dubl Philos Mag J Sci*. 1942;33(220):384-397.
42. Wicke E, Eigen M. Über den Einfluß des Raumbedarfs von Ionen in wäßriger Lösung auf ihre Verteilung in elektrischen Feld und ihre Aktivitätskoeffizienten. *Z Elektrochem Ber Bunsenges Phys Chem*. 1952;56(6):551-561.
43. Eigen M, Wicke E. The thermodynamics of electrolytes at higher concentration. *J Phys Chem*. 1954;58(9):702-714.
44. Freise V. Zur theorie der diffusen doppelschicht. *Z Elektrochem Ber Bunsenges Phys Chem*. 1952;56(8):822-827.
45. Yu Y-X, Wu J. Structures of hard-sphere fluids from a modified fundamental-measure theory. *J Chem Phys*. 2002;117(22):10156-10164.
46. Roth R, Evans R, Lang A, Kahl G. Fundamental measure theory for hard-sphere mixtures revisited: the white bear version. *J Phys Condens Matter*. 2002;14(46):12063-12078.
47. Tang W, Yu H, Zhao T, Qing L, Xu X, Zhao S. A dynamic reaction density functional theory for interfacial reaction-diffusion coupling at nanoscale. *Chem Eng Sci*. 2021;236:116513.
48. Shandilya A, Schwarz K, Sundararaman R. Interfacial water asymmetry at ideal electrochemical interfaces. *J Chem Phys*. 2022;156(1):014705.
49. Schmickler W. A unified model for electrochemical electron and ion transfer reactions. *Chem Phys Lett*. 1995;237(1):152-160.
50. Schmickler W. A theory of adiabatic electron-transfer reactions. *J Electroanal Chem Interfacial Electrochem*. 1986;204(1):31-43.
51. Santos E, Koper MTM, Schmickler W. Bond-breaking electron transfer of diatomic reactants at metal electrodes. *Chem Phys*. 2008;344(1):195-201.
52. Melander MM. Grand canonical rate theory for electrochemical and electrocatalytic systems I: general formulation and proton-coupled electron transfer reactions. *J Electrochem Soc*. 2020;167(11):116518.
53. Sakaushi K, Kumeda T, Hammes-Schiffer S, Melander MM, Sugino O. Advances and challenges for experiment and theory for multi-electron multi-proton transfer at electrified solid–liquid interfaces. *Phys Chem Chem Phys*. 2020;22(35):19401-19442.
54. Navrotskaya I, Soudackov AV, Hammes-Schiffer S. Model system-bath Hamiltonian and nonadiabatic rate constants for proton-coupled electron transfer at electrode-solution interfaces. *J Chem Phys*. 2008;128(24):244712.
55. Ávila M, Juárez MF, Santos E. Role of the partial charge transfer on the chloride adlayers on Au(100). *ChemElectroChem*. 2020;7(20):4269-4282.
56. Hörmann NG, Reuter K. Thermodynamic cyclic voltammograms based on *ab initio* calculations: Ag(111) in halide-containing solutions. *J Chem Theory Comput*. 2021;17(3):1782-1794.
57. Daikhin L, Kornyshev A, Urbakh M. Double-layer capacitance on a rough metal surface. *Phys Rev E*. 1996;53(6):6192-6199.
58. Daikhin L, Kornyshev A, Urbakh M. Nonlinear Poisson–Boltzmann theory of a double layer at a rough metal/electrolyte interface: a new look at the capacitance data on solid electrodes. *J Chem Phys*. 1998;108(4):1715-1723.
59. Trasatti S, Petrii O. Real surface area measurements in electrochemistry. *J Electroanal Chem*. 1992;327(1–2):353-376.
60. Le J, Cuesta A, Cheng J. The structure of metal–water interface at the potential of zero charge from density functional theory-based molecular dynamics. *J Electroanal Chem*. 2018;819:87-94.
61. Aslyamov T, Sinkov K, Akhatov I. Electrolyte structure near electrodes with molecular-size roughness. *Phys Rev E*. 2021;103(6):L060102.
62. Tran B, Janik MJ, Milner ST. Hydration-shell solvation and screening govern alkali cation concentrations at electrochemical interfaces. *J Phys Chem C*. 2024;128:20559-20568.
63. Tao J, Rappe AM. Physical adsorption: theory of van der Waals interactions between particles and clean surfaces. *Phys Rev Lett*. 2014;112(10):106101.
64. Silvestrelli PL, Ambrosetti A. Van Der Waals-corrected density functional theory simulation of adsorption processes on Noble-metal surfaces: Xe on Ag(111), Au(111), and Cu(111). *J Low Temp Phys*. 2016;185(1):183-197.
65. Heinz H, Vaia RA, Farmer BL, Naik RR. Accurate simulation of surfaces and interfaces of face-centered cubic metals using 12–6 and 9–6 Lennard–Jones potentials. *J Phys Chem C*. 2008;112(44):17281-17290.
66. Peng Z, Ewig CS, Hwang M-J, Waldman M, Hagler AT. Derivation of class II force fields. 4. van der Waals parameters of alkali metal cations and halide anions. *J Phys Chem A*. 1997;101(39):7243-7252.
67. Huang J. Zooming into the inner Helmholtz plane of Pt(111)–aqueous solution interfaces: chemisorbed water and partially charged ions. *JACS Au*. 2023;3(2):550-564.
68. Chen X, McCrum IT, Schwarz KA, Janik MJ, Koper MTM. Co-adsorption of cations as the cause of the apparent pH dependence of hydrogen adsorption on a stepped platinum single-crystal electrode. *Angew Chem Int ed*. 2017;56(47):15025-15029.
69. Rizo R, Fernández-Vidal J, Hardwick LJ, et al. Investigating the presence of adsorbed species on Pt steps at low potentials. *Nat Commun*. 2022;13(1):2550.

SUPPORTING INFORMATION

Additional supporting information can be found online in the Supporting Information section at the end of this article.

How to cite this article: Tang W, Zhao S, Eikerling M, Huang J. Low Parsons–Zobel slope of metal–solution interfaces: A theoretical comparison of three causes. *AIChE J*. 2026;72(2):e70133. doi:10.1002/aic.70133